Prediction-Based Auralization of a Multirotor Urban Air Mobility Vehicle

Siddhartha Krishnamurthy[1] and Stephen A. Rizzi[2]
NASA Langley Research Center, Hampton, VA, 23581, USA

Rui Cheng[3]
National Institute of Aerospace, Hampton, VA, 23681, USA

D. Douglas Boyd, Jr.[4] and Andrew Christian[5]
NASA Langley Research Center, Hampton, VA, 23681, USA

Recent advances in auralization methods applicable to rotary wing vehicles have made it possible to undertake a prediction-based auralization of a representative multirotor urban air mobility vehicle. These advances include a new capability for synthesizing loading and thickness noise directly from the prediction method and a new capability for predicting and synthesizing modulating broadband self noise within a unified system noise prediction-auralization framework. These capabilities are demonstrated for a six-passenger quadrotor reference vehicle design using collective-pitch control. Propagation of the source noise to a ground observer completes the auralization process. The demonstrated capability serves as the basis for future work directed at perception-influenced design of low noise urban air mobility vehicles.

I. Introduction

Urban Air Mobility (UAM) is an opportunity for aviation to improve transportation systems across the world. Representative UAM vehicle attributes include electrical vertical takeoff and landing (eVTOL), capacity for up to 6 passengers (or equivalent cargo), some degree of autonomy, capability of performing missions of up to 100 nautical miles at altitudes up to 3000 ft. above ground level, flight speeds up to 200 knots, and weight between 800 and 8000 pounds. For the present work, the vertical lift attribute is provided by a combination of rotors.

Several barriers, including noise, stand in the way of the many anticipated benefits of UAM. At present, there is no consensus on what constitutes an acceptable measure of noise. Nor is it clear what particular design features are necessary to achieve acceptable noise. Achieving a low noise design is also difficult because unconventional aircraft configurations introduce new noise sources, either directly by the propulsion system or indirectly by its integration on the aircraft. Unlike large commercial transports, those sources often exhibit unsteadiness on multiple time scales.

At this time, noise signatures from actual vehicles are not widely accessible to the community to help address these questions [1]. Auralization of air vehicle noise [2] is one possible means of addressing this gap by providing a means of communicating noise impact to stakeholders in a natural form, providing feedback to the noise analyst regarding the system under design, and serving as an integral element of perception-influenced design [3] of new air vehicles.

This paper demonstrates auralization of noise from rotors of a reference multirotor urban air mobility vehicle during a vehicle flyover. Two types of rotor noise will be auralized: 1. periodic loading and thickness noise and 2. broadband self noise. Periodic loading and thickness noise arise from periodic forces on rotor blades, such as lift and

[1] Research Engineer, Structural Acoustics Branch, AIAA Senior Member.
[2] Senior Researcher for Aeroacoustics, Aeroacoustics Branch, AIAA Fellow.
[3] Senior Research Engineer.
[4] Research Engineer, Aeroacoustics Branch.
[5] Research Engineer, Structural Acoustics Branch.

drag, during rotor rotation. They are calculated with solutions to the Ffowcs Williams-Hawkings (FW-H) equation [4] using the aerodynamic forces and rotor geometry. Rotor/propeller self noise is generated by the interaction of a blade airfoil encountering smooth inflow and the turbulence produced in its own boundary layer and wake space [5, 6]. The wake space occurs immediately after the blade trailing edge away from the blade motion direction. Further information on self noise generating mechanisms can be found in Refs. [5] and [6]. Self noise is considered as broadband noise, and self noise peak sound pressure levels can be between 1 kHz and 10 kHz [6].

Paper contents are as follows. First, the reference multirotor urban air mobility vehicle is introduced. The paper then discusses the noise prediction process for the vehicle's rotors, inclusive of periodic loading and thickness noise and broadband self noise. The process for synthesizing the source noise, that is, converting the source noise prediction to an acoustic pressure time history, is reviewed. Emphasis is placed on describing the self noise synthesis process. Finally, auralizations of level cruise maneuvers with different trailing edge blade thicknesses are made to demonstrate how the vehicle noise changes with emission angle and with different rotor blade designs.

II. Aircraft and Flyover Descriptions

A. Aircraft Description

The eVTOL vehicle selected for this study is a six passenger, 1200 lb payload quadrotor turboelectric design [7], depicted in Fig. 1, with the right side of the figure showing a transparent view of the aircraft interior. The vehicle was developed using the NASA Design and Analysis of Rotorcraft (NDARC) code [8] and uses collective control due to the large radii (13.10 ft (3.99 m)) of the rotors. The version of the quadrotor vehicle used in this work has three blades on each rotor. The rotation speed of each rotor is roughly 400 revolutions per minute giving a blade passage frequency of approximately 20 Hz. The rotor numbers are labeled on the right side of Fig. 1. Rotors 1 and 3 rotate counter-clockwise (CCW) with respect to a view above and forward to the vehicle. Rotors 2 and 4 rotate clockwise (CW).

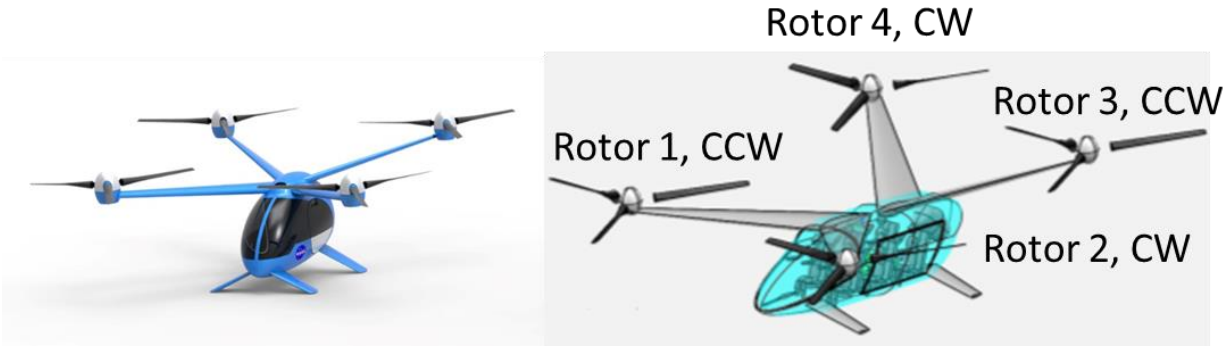

Fig. 1 Six-passenger reference eVTOL quadrotor vehicle.

The trailing edge thickness of the rotor blades affects the self noise emitted from the rotors. In this work, vehicle auralizations with four trailing edge thicknesses will be presented: 0.9 mm, 1.8 mm, 3.6 mm, and 7.2 mm.

B. Flyover Description

Parameters for a simulated flyover of the eVTOL Quadrotor are given in Fig. 2. The flyover sound will be audible, or auralized, at the ground observer. The flyover trajectory considered in this work is only along the x and z axes and is straight and level with constant velocity. Positive x is toward the front of the vehicle, and positive z is upward. As shown by the axes label in Fig. 2, the positive y axis is into the page. From some initial position, the vehicle is given a velocity, V. The parameter V entirely specifies the flight condition. The climb angle would also specify the flight condition, but in this work the climb angle is zero degrees. Parameter D_1 specifies the ground range from the vehicle's initial position to the ground observer. The flyover lasts until the vehicle is at a final ground range position, D_2, from the ground observer. The parameter H is the vehicle altitude. The vehicle has a pitch about its center of gravity, θ_p, with positive pitch indicating pitch nose up. The vehicle also contains a roll angle about the x axis, but the roll angle is not represented in Fig. 2.

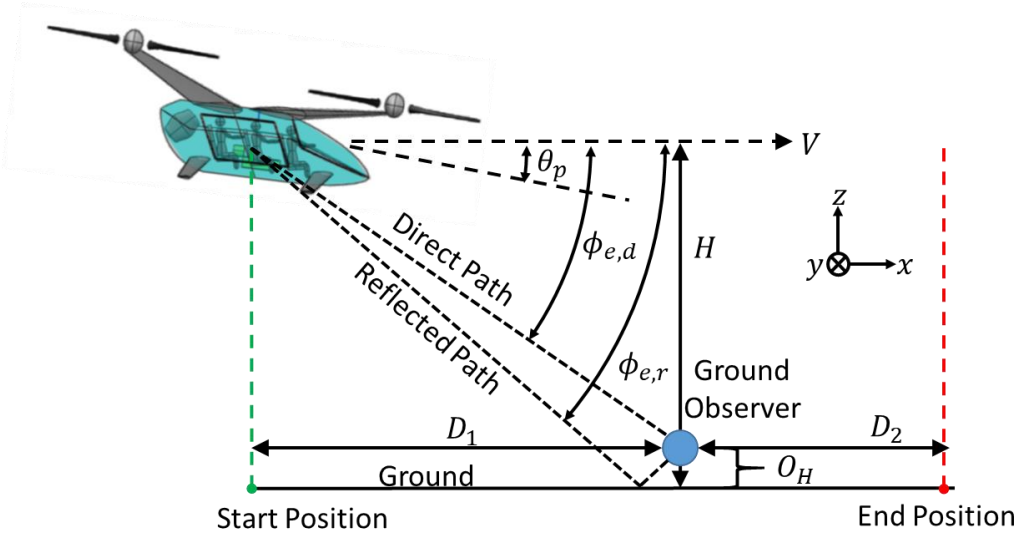

Fig. 2 Flyover parameters.

Sound emitted from the vehicle to a ground observer with height O_H will follow direct and ground-reflected paths. The ground observer is stationary. The emission angle from the vehicle to the ground observer for the direct path is labeled $\phi_{e,d}$ in Fig. 2. The emission angle for the reflected path is labeled $\phi_{e,r}$. These emission angles change with time as the vehicle flies. If $O_H = 0$, then the direct and reflected paths are identical, the direct and ground-reflected emission angles are identical, and the sound pressure at the ground observer is double the sound pressure (for hard ground surface) received at the observer from the direct path.

The auralization examples in this work have straight and level flyovers with a velocity of $V = 90$ knots true air speed (KTAS) at an altitude of $H = 1000$ ft (304.8 m). The auralizations are 25 seconds long with the vehicle above the ground observer at 12.5 seconds, which corresponds to $D_1 = D_2 = 0.36$ miles (579.36 m). The vehicle is pitched down at $\theta_p = -7.19°$ and the vehicle roll angles are considered negligible and are approximated to be 0°. The ground observer is flush with the rigid ground where $O_H = 0$ meters.

III. Auralization Overview and Input Data

A. Auralization Process

The auralization process consists of a series of steps, and a flowchart of the basic process is given in Fig. 3. These steps are used to auralize separate noise sources on the vehicle individually before summing their contributions [2]. This method is useful when a vehicle has distributed noise sources, each with significantly different emission angles to the ground observer. For this work, the separate noise sources are the four rotors of the eVTOL quadrotor. Installation effects and other noise sources, e.g., electric motor or turbomachinery noise, are not included in this work. Auralization steps presented in Fig. 3 are applied to each rotor. The sounds from all the rotors are summed at the ground observer to complete the auralization.

The first three auralization steps all occur at or near each rotor. There is no standard definition of what distance may be considered near a rotor, but this work is interested in generating far field acoustics. Steps 1 and 2 (blue and green boxes in Fig. 3, respectively) form a source noise definition. Source noise definitions can originate from various methods, including computational analyses, or ground and flight test measurements when available. If computational analyses are used, Step 1 is to produce data for the rotor blades such as blade loadings and blade inflow velocity. With these data, sound pressures are predicted near a rotor to form the source noise definition. Acoustic predictions forming a source noise definition are not necessarily in a form that are audible. Source noise synthesis in Step 3 (brown box in Fig. 3) transforms the acoustic predictions into audible sound, or acoustic pressure time history, emitted from the source along a set of time-varying source emission angles.

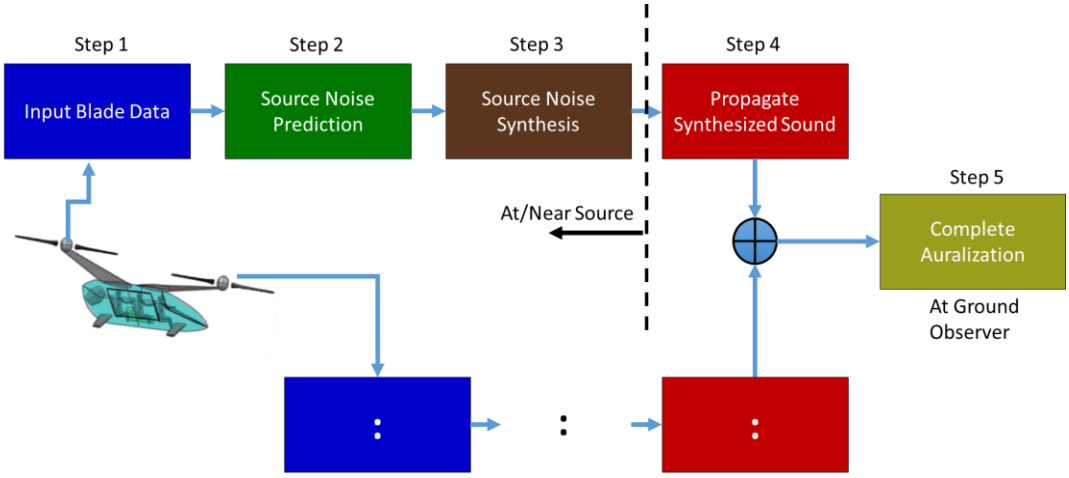

Fig. 3 Auralization steps.

In Step 4 (red box in Fig. 3), propagation effects are applied to the synthesized sound. These effects include spreading loss, atmospheric absorption, and time delay or Doppler. Contributions from multiple propagation paths may be included, although for an observer flush with the ground, the contributions are identical.

The general auralization steps 1-4 in Fig. 3 for each rotor will be applied separately to each type of noise. Since this paper will auralize the rotor periodic and broadband self noise sounds, the general steps in Fig. 3 will be demonstrated for periodic noise and then applied again for the broadband self noise. Step 5 (yellow-green box in Fig. 3) sums the propagated periodic and broadband components with contributions from all the rotors to complete the auralized sound of the vehicle at the ground observer.

B. Blade Input Data

In this work, computational analyses are used to obtain the blade input data as the first step in the auralization process. For a prescribed flight condition, defined by the velocity, V, from Fig. 2, the Comprehensive Analytical Rotorcraft Model of the Rotorcraft Aerodynamics and Dynamics (CAMRAD II) program [9] is used to obtain the corresponding vehicle state, including collective, orientation, motor speed (rotor or motor, but rotor speed is predetermined and not obtained by CAMRAD II), and corresponding aerodynamics and blade motion. This trim operation is performed in a quasistatic sense to obtain the blade loadings and motion needed to predict periodic noise and blade inflow velocity and effective angle of attack needed to predict self noise. The operation is depicted in Fig. 4.

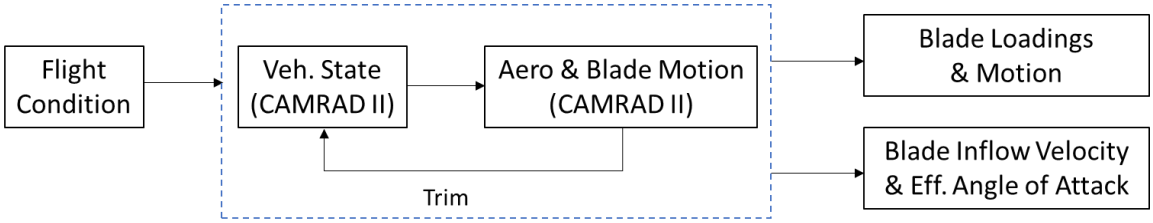

Fig. 4 Operations to obtain input data to noise calculations.

IV. Periodic Sound Synthesis

A. Periodic Sound Synthesis Process

Periodic sound synthesis in this work uses the recently developed NASA Auralization Framework (NAF) [10] F1A Synthesis Plugin [11, 12]. Steps 2 and 3 from Fig. 3, source noise prediction and synthesis, are both encapsulated in this plugin. This plugin calculates periodic noise sound pressures from the vehicle rotors using Farassat's formulation 1A (F1A) [13], which is a solution to FW-H equation [4]. Given the blade loadings, motion, and geometry data from CAMRAD II, the NAF F1A Synthesis Plugin uses the NASA Aircraft Noise Prediction Program 2

(ANOPP2) [14] Formulation 1A Internal Function Module (AF1AIFM) for the F1A calculations. See Ref. [12] for details on how the NAF uses AF1AIFM.

The NAF F1A Synthesis plugin computes rotor noise periodic sound pressures at a fixed distance from the source at each time sample at the instantaneous emission angle between the rotor and the ground observer. These sound pressures form a tracking observer. Further description of the tracking observer can be found in Ref. [12]. Tracking observer sample rates do not have to equal the auralization sample rate of 44.1 kHz, but they must be high enough to include relevant source frequency content. The F1A Synthesis plugin subsequently upsamples the tracking observer sample rate to 44.1 kHz. Separate tracking observers are required for each rotor. In general, separate tracking observers are also required for each propagation path, but for an observer flush with the ground the tracking observers for the direct and ground-reflected paths are identical.

The tracking observer maintains a constant distance from the moving rotor. This distance should be large enough to eliminate near field effects from contributing significantly to the F1A calculation. The constant distance from the source eliminates Doppler effects from appearing in the tracking observer sound pressures. The F1A calculations do not include atmospheric attenuation and ground-reflections, and these effects are not present in the tracking observer sound pressure calculations. After the tracking observer calculations are complete, the NAF F1A Synthesis plugin scales and time shifts the tracking observer pressures to a distance of one meter from the rotor to complete generation of the synthesized sound. Further details on these processes are described in Ref. [12]. The NAF propagates the synthesized sound pressures from each rotor to a ground observer to complete the auralization with just the periodic sound contribution [12].

B. Periodic Sound Synthesis Results

The F1A Synthesis plugin performed periodic sound synthesis for the four rotors of the eVTOL quadrotor using tracking observers with a sample rate of 8820 Hz at 100 meters from the rotors for the flyover scenario in Fig. 2. Section II.B mentions that this paper presents vehicle flyover auralizations with different blade trailing edge thicknesses. Unlike for self noise, which will be discussed shortly, rotor periodic noise did not change with the different blade trailing edge thicknesses. The synthesized sound for Rotor 1 is shown in Fig. 5 after scaling and time shifting the tracking observer sound pressures to a distance of one meter from the rotor and upsampling the pressures to 44.1 kHz. The results in Fig. 5 are before propagation effects were applied. The left trace in Fig. 5 is the synthesized acoustic pressure time history. Figure 5 also shows the corresponding spectrogram on the right plot. Since Doppler effects are not present in the tracking observer, the spectrogram contains horizontal lines corresponding to harmonics of the approximately 20 Hz blade passage frequency.

The elevation and azimuth emission angles from the rotor to the ground observer as a function of time are given in the bottom two plots. Note the azimuth emission angles are less than zero degrees because Rotor 1 was on the starboard side of the vehicle with respect to its center of gravity as shown in Fig. 1. The center of gravity was along the centerline to the ground observer. Since the observer is flush with the ground, propagation paths 1 and 2 corresponding to the direct and reflected paths were identical.

Green and blue lines appear to sweep across time and frequency in the spectrogram in a comb pattern in Fig. 5. These patterns are not evidence of unintended reflections or Doppler effects in the synthesis. Reference [12] describes the source of these comb patterns as coming from the blade input data or the F1A calculation and not from the synthesis.

Figure 6 provides a magnified view of the synthesized time history and corresponding spectrogram, clarifying the rotor blade passages. The synthesis results for the other three rotors are similar, but not identical, to the Rotor 1 results in Figs. 5 and 6, and are not shown.

V. Broadband Self Noise Synthesis Overview

A. Previous Broadband Self Noise Synthesis Efforts

Broadband self noise generated by rotorcraft blades has long been known to contain amplitude modulations at the blade passage frequency [15]. In Ref. [16], these modulations were shown to be salient to the audible sound produced by self noise. A preliminary broadband self noise synthesis method that accounted for the modulations was developed in Ref. [16], but the sound was produced for a single emission angle and not for a full aircraft flyover spanning a range of emission angles. Reference [17] found the modulations from recorded self noise to be important and contribute to the roughness sound quality of the audible self noise sound.

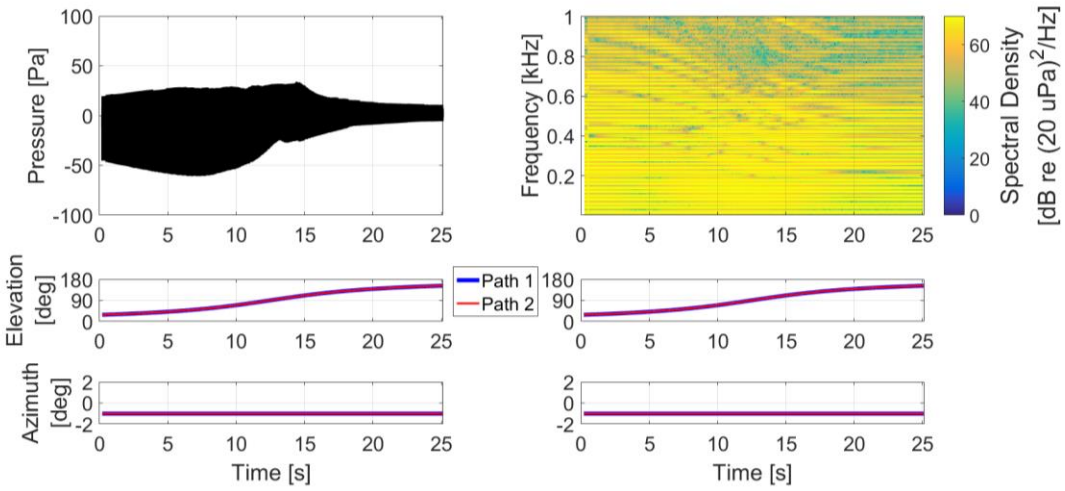

Fig. 5 Synthesized periodic sound of Rotor 1.

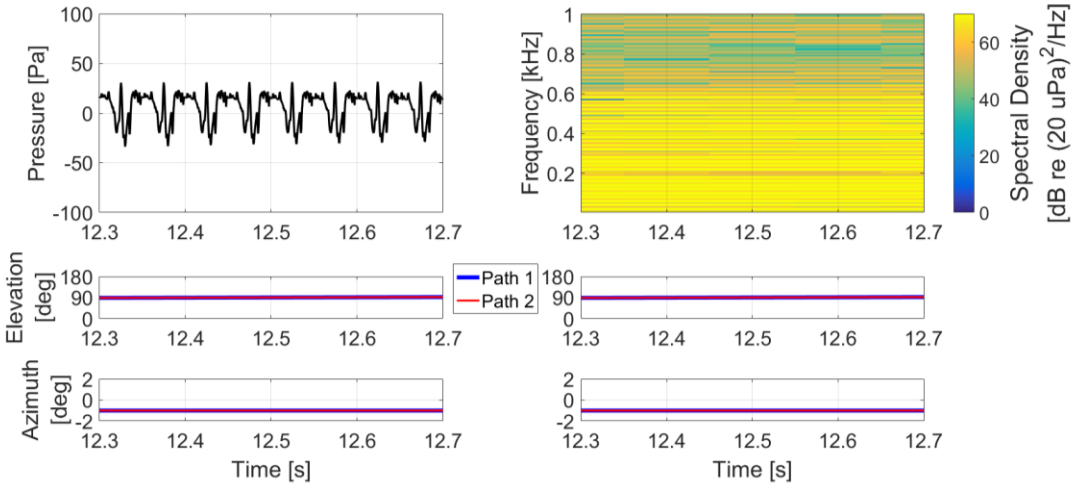

Fig. 6 Magnified synthesized periodic sound of Rotor 1.

B. Self Noise Synthesis and Auralization Process Overview

This paper presents the development of a broadband self noise synthesis method that reproduces the amplitude modulations for a full flyover spanning multiple emission angles. Auralizations of the broadband self noise from the eVTOL quadrotor flyovers follow the general steps in Fig. 3, but Fig. 7 provides details specific to the self noise auralization for a single rotor. From Step 1, blade inflow velocity, effective angle of attack, and blade geometry from CAMRAD II are input to Step 2, broadband self noise prediction. Step 2 uses the ANOPP2 Self Noise Internal Functional Module (ASNIFM), which combines computational and empirical analyses to quickly compute self noise from the trailing edge of a rotor blade using frequency domain data in Ref. [5]. This approach is commonly referred to as the Brooks, Pope, and Marcolini self noise model in a rotating frame. In Step 3, the self noise from the rotor to be emitted to the ground observer is then synthesized using the predictions from ASNIFM. This synthesis process will be described in Sections VI and VII. Unlike periodic noise synthesis, which is executed using the NAF F1A Synthesis plugin, the self noise synthesis is not currently executed within a NAF plugin. This paper demonstrates a proof of concept for the self noise synthesis method as a first step to developing it into a NAF plugin. For this reason, the self noise synthesis method is designated as a prototype process. The NAF is only utilized in Step 4, which accepts the synthesized self noise as input and applies propagation effects toward the ground observer. Step 5 combines the propagated self noise contributions from all rotors.

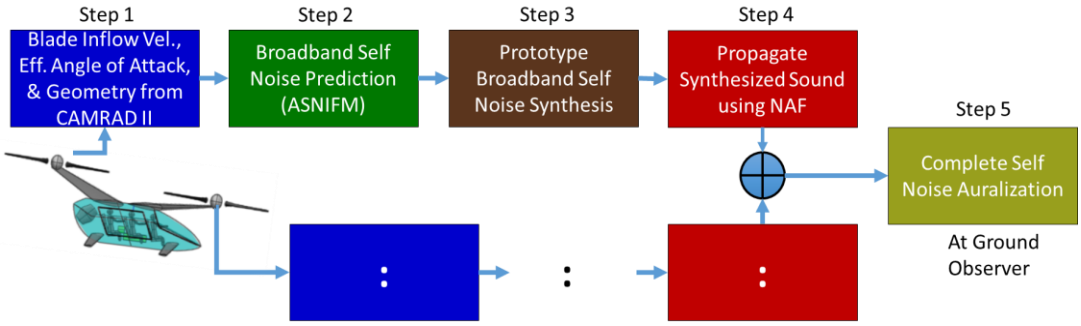

Fig. 7 Self noise auralization steps.

C. Broadband Self Noise Data

ASNIFM presents self noise predictions as 1/3 octave band sound pressure level magnitude time histories emitted over one rotor revolution at a set of evenly spaced discrete points on a hemisphere at some radial distance from the rotor noise source. This hemisphere around the rotor is referred to as a source noise hemisphere. Figure 8 gives an example of the source noise hemisphere. A rotor with three blades is seen in the middle of the hemisphere. The hemisphere radius is typically much larger in implementation than what is seen in Fig. 8, which has a small radius relative to rotor radius for illustration purposes. The center of the source noise hemisphere must be centered around each rotor. Rotor displacement from vehicle pitch and roll must be accounted for in the hemisphere centering.

Intersections of the hemisphere mesh grid lines represent self noise prediction points with the spatial coordinate of each point defined by an emission angle. The data from two of the points, corresponding to two different emission angles, are shown. The data format is similar to that of a spectrogram, but the vertical axis is the 1/3 octave band number. Data at each 1/3 octave band are given for a nominal center frequency. Band 30, for example, is centered at 1 kHz, and band 40 is centered at 10 kHz. At each 1/3 octave band center frequency, the mean square of the sound pressures, or sound pressure levels, are computed using ASNIFM at a user-specified sample rate. In the Fig. 8 example, the sample rate is approximately 434 Hz. ASNIFM data are provided in the decibel scale with respect to 20 µPa squared. At the higher 1/3 octave band frequencies (above about band 20), one can see lobes of high sound pressure levels separated by the 20 Hz rotor blade passages. These lobes are responsible for the modulations salient to the audible self noise. Predicted data at all time steps at a single spatial point on the hemisphere correspond to that point's particular emission angle. Since the predictions are only a rotor revolution in duration and, more importantly, only contain sound pressure level magnitude information at 1/3 octave band center frequencies and no narrowband phase information, they cannot directly produce the audible self noise, hence the need for a separate sound synthesis process.

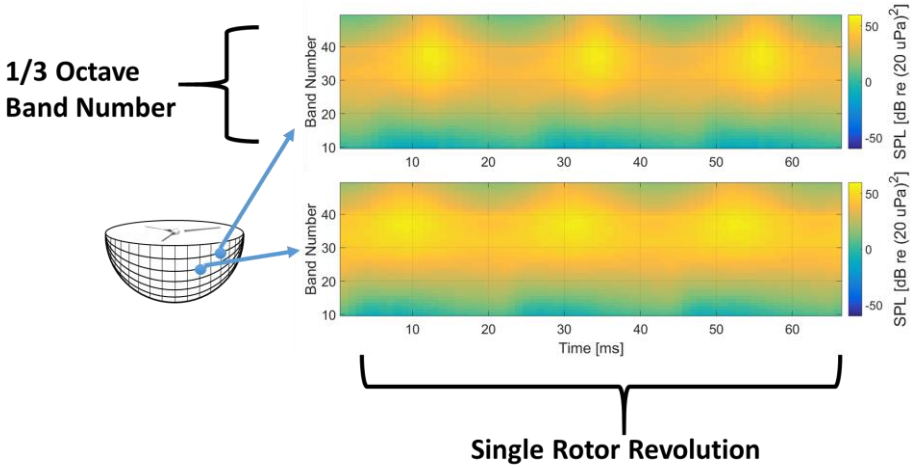

Fig. 8 Broadband self noise sound pressure predictions.

D. Self Noise Synthesis Steps

Synthesizing self noise audible sound pressures for rotorcraft flyovers from the ASNIFM data involves two main steps:

1) Extend the self noise data over multiple rotor revolutions to span the full vehicle flyover duration.
2) Modulate a stochastic signal by the extended self noise data.

VI. Self Noise Synthesis Step 1: Extending Data

To extend the self noise data, emission angles as a function of time for the full flyover duration from rotor to ground observer are first found from the vehicle trajectory and the ground observer position. Figure 9 illustrates the determination of emission angles using an exaggerated discretization. Here, the emission angles at three consecutive time samples, t_A, t_B, and t_C are found. In this example, the azimuth emission angle, ϕ, remains constant at the three time samples, but the elevation emission angles, θ_A, θ_B, and θ_C, change at time samples t_A, t_B, and t_C, respectively. The emission angles are given as a function of time in the bottom right plot in Fig. 9. At times t_A and t_C, the emission angles correspond to prediction points on the source noise hemisphere. At time t_B, the emission angle falls on a point on the source noise hemisphere that is between prediction points.

Self noise sound pressure level magnitudes at each 1/3 octave band center frequency are interpolated over time through points on the source noise hemisphere corresponding to the flyover emission angles. The resulting interpolated sound pressure level data correspond to multiple rotor revolutions as the emission angle moves through multiple points on the source noise hemisphere. Figure 10 provides an illustration of the interpolation using the emission angles found in Fig. 9. Data at prediction points with emission angles θ_A and θ_C are represented on the left side of Fig. 10 by the matrices labeled Data_A and Data_C, respectively. The horizontal axes are time over one rotor revolution and the vertical axes are 1/3 octave band numbers. If the rotor in Fig. 10 is hovering at the position with respect to the ground observer given for time t_A, then the sound pressure level data are simply a repetition of Data_A as shown on the right side of Fig. 10.

The first column of Data_A occurs at time step t_A for hover as shown by the extended Data_A matrix on the top left of Fig. 10. Therefore, this column is placed in the Extended Data for Flyover matrix at time step t_A in the bottom left of Fig. 10. Similarly, at time step t_C, the emission angle for a moving rotor is θ_C. The third column of Data_C occurs at time step t_C when the rotor is hovering and maintaining the emission angle θ_C with the ground observer. The third column of Data_C is placed in the Extended Data for Flyover matrix at time step t_C. When the rotor is at time step t_B, the emission angle is θ_B; the data at time t_B is found by linearly interpolating data from the extended Data_A and the extended Data_C matrices. Before data are interpolated, they are converted from decibel to linear scale, and the square root of the data are taken to generate root mean square sound pressure values. After interpolation, data are subsequently converted back to mean square values in the decibel scale with respect to 20 µPa squared. As illustrated in Fig. 10, this interpolated data column is placed at time t_B in the Extended Data for Flyover matrix.

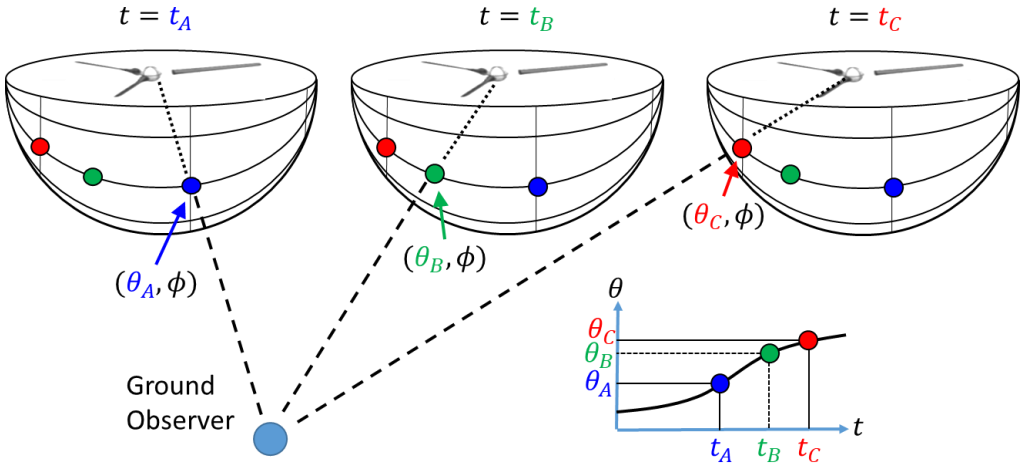

Fig. 9 Finding emission angles as a function of flyover time.

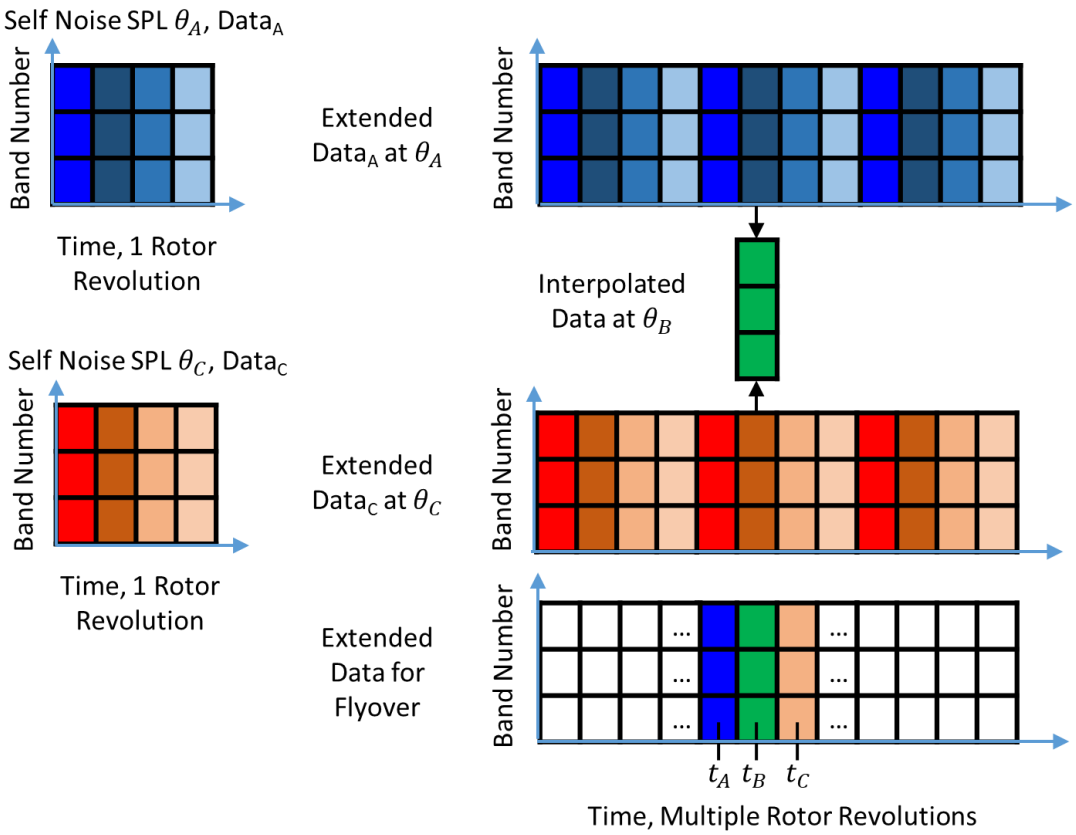

Fig. 10 Generating extended self noise data with interpolation.

Figure 11 gives an example result of applying the self noise data extension process to ASNIFM data. The result in Fig. 11 is for Rotor 1 of the eVTOL quadrotor and for the flyover in Fig. 2. The result is magnified to be between 2 and 3 seconds on the left plot and between 12 and 13 seconds on the right plot, corresponding to emission angles near the beginning and middle of the flyover, respectively. The azimuth emission angle is constant. Sound pressure level lobes across multiple rotor revolutions are visible. These lobes are roughly identical over a small range of emission angles but change significantly over long duration. Data between bands 29 and 40 (nominal center frequencies 800 Hz to 10 kHz) contain reduced modulation for emission angles corresponding to the middle of the flyover in the right plot of Fig. 11. There is no previous reference to check the modulation change in the ASNIFM data with emission angle for the eVTOL quadrotor rotors.

Since the extended data still only contain sound pressure level magnitude information at 1/3 octave band center frequencies and no narrowband phase information, they also cannot directly produce the audible self noise.

VII. Self Noise Synthesis Step 2: Modulating a Stochastic Signal

An acoustic pressure time history of the self noise is generated in the self noise synthesis process by modulating a bandlimited stochastic signal by the extended self noise data. Broadband noise source synthesis, such as for jet noise synthesis, can be accomplished by assigning independent and identically distributed random phases to narrowband frequencies in the noise spectrum [2]. This characteristic of spectrum phases will be assumed for synthesizing the broadband self noise in this work. Section VIII.B will discuss the appropriateness of this choice of a stochastic signal.

Figure 12 gives a flowchart of the steps (in green) and variables (in red) for modulating a stochastic signal to generate the synthesized self noise. Notional time histories, in Pascals, of the output and input of the different steps are given by the blue traces. The “0” on the left of each trace shows where an amplitude of zero Pascals occurs, and it indicates if the trace amplitudes are only nonnegative or if they may obtain negative values.

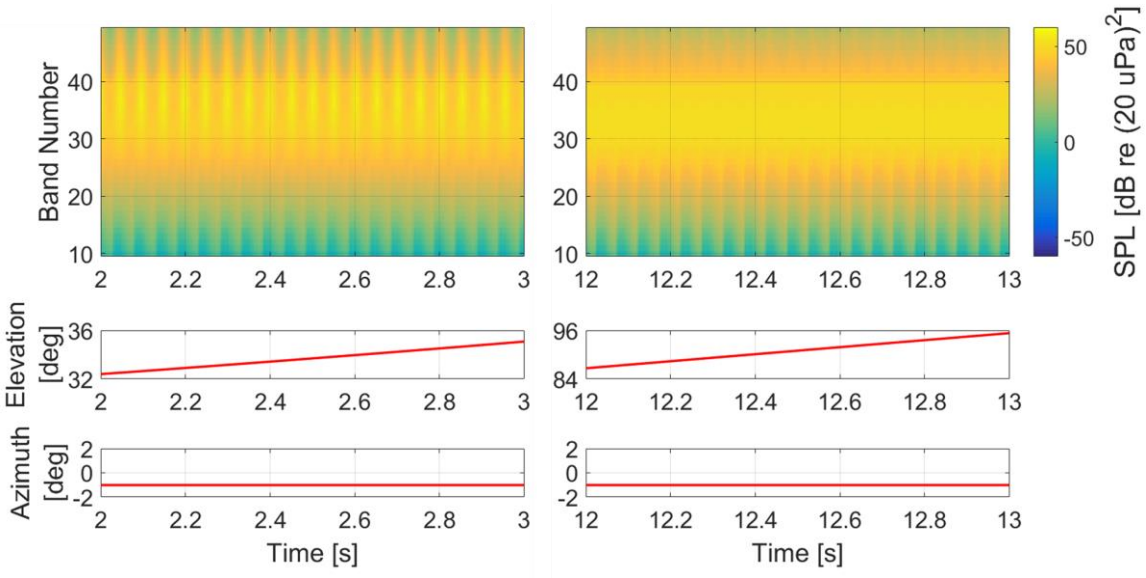

Fig. 11 Extended ASNIFM self noise data, Rotor 1, 1.8 mm trailing edge thickness.

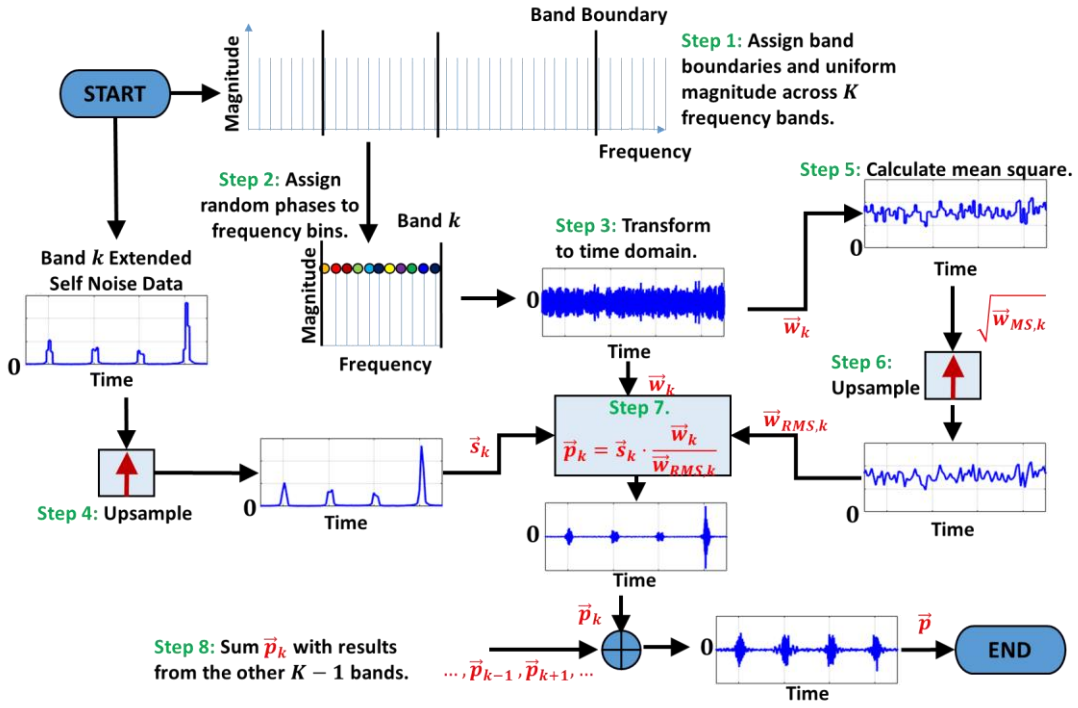

Fig. 12 Flowchart of stochastic signal modulation.

Step 1 in Fig. 12 begins building the stochastic signal in the frequency domain by dividing the stochastic signal spectrum into nonoverlapping 1/3 octave bands. Let the stochastic signal have a sample rate f_s. Although it is not necessary, it is convenient to choose the value of f_s to be 44.1 kHz, the audio sample rate, and this value was chosen in this work. Let the number of stochastic signal samples be N. The value of N is chosen so that N/f_s is the duration of the flyover, but it will be discussed shortly how N can be a smaller value. Let N_f be the number of nonnegative frequencies in the discrete Fourier transform of the stochastic signal. If N is an even number, $N_f = \frac{N}{2} + 1$. Each element, i, of the nonnegative frequency vector, $\vec{f}$, is given by

$$\vec{f}[i] = i \times \frac{f_s}{N} - \frac{f_s}{N}, \quad i = \{1, \ldots, N_f\} \tag{1}$$

where $i = 1$ indicates 0 Hz and $i = N_f$ corresponds to the Nyquist frequency.

The stochastic signal will be built using the same number of 1/3 octave bands as in the extended data with each element of the frequency vector in Eq. 1 assigned to a single 1/3 octave band. To uniquely assign frequencies to bands, the boundaries of the bands need to be determined. Let there be K 1/3 octave bands, let k indicate the band number, and let k_1 be the lowest band number. In Figs. 8 and 10, there are $K = 40$ 1/3 octave bands from band $k_1 = 10$ to band $k = 49$. Frequency boundaries of each band for the stochastic signal are determined using the following equations:

$$\boldsymbol{f_{c,k} = 10^{\frac{k}{10}}} \tag{2}$$

$$\boldsymbol{f_{1,k} = f_{c,k} - \alpha \cdot f_{c,k} \cdot \frac{10^{0.05}}{2} + \frac{f_{c,k}}{2 \cdot \alpha \cdot 10^{0.05}}} \tag{3}$$

$$\boldsymbol{\alpha = \begin{cases} 0.995, & \frac{f_{c,k}}{f_s} \leq 0.25 \\ 0.998 & \frac{f_{c,k}}{f_s} > 0.25 \end{cases}.} \tag{4}$$

In Eqs. 2-4, for each 1/3 octave band, k, $f_{c,k}$ is the center frequency and $f_{1,k}$ is the first frequency. The true first frequency in band k will be the minimum frequency in $\vec{f}$ greater than or equal to $f_{1,k}$. The last frequency in band $k < (K + k_1 - 1)$ is the maximum frequency in $\vec{f}$ less than $f_{1,k+1}$. The maximum frequency in the highest band, $k = (K + k_1 - 1)$, is bounded above by

$$\boldsymbol{f_{2,K+k_1-1} = f_{c,K+k_1-1} + \alpha \cdot f_{c,K+k_1-1} \cdot \frac{10^{0.05}}{2} - \frac{f_{c,K+k_1-1}}{2 \cdot \alpha \cdot 10^{0.05}}}. \tag{5}$$

The value of α in Eq. 5 is given by Eq. 4. Center frequencies computed from Eq. 2 do not necessarily correspond exactly to the center frequencies used by ASNIFM, but the center frequency differences have negligible effect on assigning band boundaries.

In each 1/3 octave band, k, Steps 1 and 2 in Fig. 12 assign uniform magnitude and random phase, respectively, over the frequency bins. The magnitude and phase in band k and each frequency bin i is:

$$\boldsymbol{W_{k,i} = \begin{cases} 0, & \vec{f}[i] < f_{1,k}, & k_1 \leq k \leq (K + k_1 - 1) \\ \frac{\sqrt{N}}{f_s} e^{j2\pi\phi_i}, & f_{1,k} \leq \vec{f}[i] < f_{1,k+1}, & k_1 \leq k < (K + k_1 - 1) \\ \frac{\sqrt{N}}{f_s} e^{j2\pi\phi_i} & f_{1,k} \leq \vec{f}[i] \leq f_{2,k}, & k = (K + k_1 - 1) \\ 0, & \vec{f}[i] \geq f_{1,k+1}, & k_1 \leq k < (K + k_1 - 1) \\ 0, & \vec{f}[i] > f_{2,k}, & k = (K + k_1 - 1) \end{cases}, i = \{1, \ldots, N_f\}.} \tag{6}$$

In Eq. 6, ϕ_i is a uniformly distributed random phase variable between values of 0 and 1 that is independent over all values of i. If N is even, then $\phi_{N_f} = 0$. Note that since 1/3 octave bands do not overlap, Eq. 6 provides independently distributed phase values across different values of k and, therefore, across different bands. Eq. 6 assumes $f_{1,k_1} > 0$. The factor $\sqrt{N}/f_s$ in Eq. 6 will normalize the mean square of the stochastic signal so that it cannot be greater than one even if all 1/3 octave bands from 0 Hz to the Nyquist frequency contain nonzero frequency content.

Let there now be a vector $\vec{W}_k$ of N elements for each band k so that each element is given by

$$\boldsymbol{\vec{W}_k[m] = \begin{cases} W_{k,m}, & 1 \leq m \leq N_f \\ W^*_{k,2N_f-m+1}, & N_f < m \leq N \end{cases}.} \tag{7}$$

In Eq. 7, $W^*_{k,i}$ is the complex conjugate of $W_{k,i}$. Equation 7 is the linear spectrum of the stochastic signal in each band. In Step 3 of Fig. 12, taking the inverse discrete Fourier transform of Eq. 7 and multiplying the result by f_s will give the stochastic signal time history in each 1/3 octave band, $\vec{w}_k[n]$, with sample rate f_s and N samples. Letting the number of nonzero values of $W_{k,i}$ for each k be $N_{f,k}$, the mean square of each band k is given by

$$\boldsymbol{w_{MS,k} = \frac{2N_{f,k}}{N}}. \tag{8}$$

Step 4 in Fig. 12 upsamples the square root of the extended self noise data time history, or its root mean square time history, for 1/3 octave band k, from $f_{s,data}$, the sample rate of the extended self noise spectrum data, to f_s. The upsampling should maintain the nonnegative sound pressure level values in the data. Let $\vec{s}_k$ be the upsampled time history with sample rate f_s and with N number of samples.

To check the upsampling, let the mean square time history of $\vec{s}_k$ be recalculated using a time step of Δ_{MS}. Let N_Δ be the number of samples of $\vec{s}_k$ for each mean square calculation time step so that

$$\boldsymbol{N_\Delta = \Delta_{MS} \cdot f_s} \,. \tag{9}$$

If the mean square time history of $\vec{s}_k$ is recalculated using a time step of $1/f_{s,data}$, then it should approximate the original self noise data time history before upsampling. Since N_Δ in Eq. 9 needs to be an integer, the mean square calculation time step is given by

$$\boldsymbol{\Delta_{MS} = ri\left(\frac{f_s}{f_{s,data}}\right) \cdot \frac{1}{f_s}} \,. \tag{10}$$

In Eq. 10, $ri(x)$ means x rounded to the nearest integer. From Eqs. 9 and 10,

$$\boldsymbol{N_\Delta = ri\left(\frac{f_s}{f_{s,data}}\right)} \,. \tag{11}$$

Using Eqs. 10 and 11, let the lth mean square calculation of $\vec{s}_k$ be

$$\boldsymbol{\vec{s}_{MS,k}[l] = \frac{1}{N_\Delta}\sum_{n=N_\Delta\cdot(l-1)+1}^{N_\Delta\cdot l} \vec{s}_k^2[n]} \,. \tag{12}$$

Equation 12 should be approximately equal to the extended self noise data if the upsampling to form $\vec{s}_k$ is performed appropriately. Although $\vec{s}_k$ may have an audio sample rate, it is not yet representative of the acoustic pressure time history of self noise since it only contains nonnegative values.

A representative acoustic pressure time history of self noise is a stochastic signal of length N and sample rate f_s that contains modulations from the extended self noise data for band k and whose elements are given by

$$\boldsymbol{\vec{p}_k[n] = \vec{s}_k[n] \cdot \frac{\vec{w}_k[n]}{\vec{w}_{RMS,k}[n]}} \,. \tag{13}$$

Equation 13 is given in Step 7 of Fig. 12.

Arriving at Step 7 through Steps 5 and 6 requires the following discussion. The acoustic pressure $\vec{p}_k$ should have approximately the same mean square time history as the original extended self noise data. Let the lth mean square calculation of $\vec{p}_k$ be

$$\boldsymbol{\vec{p}_{MS,k}[l] = \frac{1}{N_\Delta}\sum_{n=N_\Delta\cdot(l-1)+1}^{N_\Delta\cdot l} \vec{s}_k^2[n] \cdot \frac{\vec{w}_k^2[n]}{\vec{w}_{RMS,k}^2[n]}} \,. \tag{14}$$

To compare the mean squares of $\vec{p}_k$ with the original data, the number of samples in a mean square calculation time step, N_Δ, is set to Eq. 11. Letting $\vec{w}_{RMS,k} = |\vec{w}_k|$ will allow the mean square of $\vec{p}_k$ to be equal to the mean square of $\vec{s}_k$, but the resulting audible sound will just contain positive, zero, or negative values of the upsampled ASNIFM data. Since the extended self noise data approximately repeats over multiple rotor revolutions over a small range of emission angles, the audible sound will not contain sound pressure level variations. Here, large sound pressure level variations refer to there being a wide distribution of sound pressure level values.

Although self noise data change over time, with Eqs. 10 and 11, an assumption is made that $\vec{s}_k$ does not change significantly within the time interval Δ_{MS} and over N_Δ samples, or

$$\boldsymbol{\vec{s}_{MS,k}[l] \approx \vec{s}_k^2[n], (N_\Delta \cdot (l-1) + 1) \le n \le N_\Delta \cdot l} \,. \tag{15}$$

From Eq. 15, Eq. 14 becomes

$$\boldsymbol{\vec{p}_{MS,k}[l] \approx \frac{\vec{s}_{MS,k}[l]}{N_\Delta}\sum_{n=N_\Delta\cdot(l-1)+1}^{N_\Delta\cdot l} \frac{\vec{w}_k^2[n]}{\vec{w}_{RMS,k}^2[n]}} \,. \tag{16}$$

If $\vec{w}_{RMS,k}$ is equal to one Pascal, then the mean square of $\vec{p}_k$ will become $\vec{s}_{MS,k}$ multiplied by the mean square of $\vec{w}_k$ in the interval Δ_{MS}, which will be a poor approximation to the original data.

Dividing $\vec{w}^2{}_k$ in Eq. 16 by $w_{MS,k}$ from Eq. 8 is a possible option, but the mean square of $\vec{w}_k$ over N_Δ samples may be significantly different from $w_{MS,k}$. Let each element of the mean square time history of $\vec{w}_k$ be

$$\vec{w}_{MS,k}[l] = \frac{1}{N_\Delta}\sum_{n=N_\Delta\cdot(l-1)+1}^{N_\Delta\cdot l} \vec{w}_k^2[n] \,. \tag{17}$$

Figure 13 shows Eq. 17 for band $k = 40$ using different values of N_Δ for every mean square calculation time step, Δ_{MS}, over four seconds. The sample rate for $\vec{w}_k$ in Fig. 13 is $f_s = 44.1$ kHz. As an example, the gray trace uses $N_\Delta = 5$ for $\Delta_{MS} = 0.11$ ms. The black dashed trace is $w_{MS,40}$ from Eq. 8. As N_Δ increases, the mean square of $\vec{w}_k$ becomes closer to $w_{MS,k}$. With the ASNIFM data in Fig. 8 having $f_{s,data} \approx 434$ Hz, we have, from Eq. 11, $N_\Delta = 102$, and many mean square samples of $\vec{w}_{MS,k}$ in Eq. 17 will not be relatively close to $w_{MS,k}$ in Eq. 8.

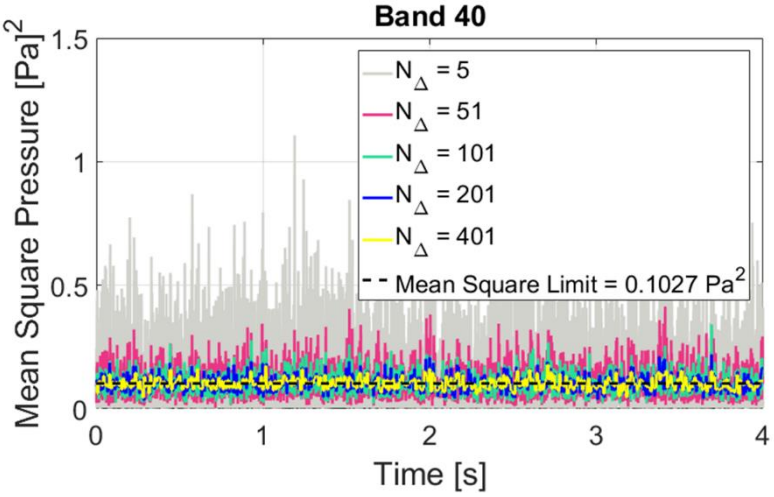

Fig. 13 Mean square of stochastic signal, $\vec{w}_k$, for band $k = 40$, $f_s = 44.1$ kHz.

Define $\vec{w}_{RMS,k}$ to be upsampled from $\sqrt{\vec{w}_{MS,k}}$ so that the upsample is from $1/\Delta_{MS}$ to f_s and that $\vec{w}_{RMS,k}$ has N samples. Along with this definition, $\vec{w}_{RMS,k}$ will be assumed approximately constant within a time interval Δ_{MS} and over N_Δ samples. Now, Eq. 16 becomes

$$\vec{p}_{MS,k}[l] \approx \frac{\vec{s}_{MS,k}[l]}{\vec{w}_{MS,k}[l]\cdot N_\Delta}\sum_{n=N_\Delta\cdot(l-1)+1}^{N_\Delta\cdot l} \vec{w}_k^2[n] \,. \tag{18}$$

Applying Eq. 17, Eq. 18 becomes

$$\vec{p}_{MS,k}[l] \approx \vec{s}_{MS,k}[l] \,. \tag{19}$$

Equation 19 shows that defining $\vec{w}_{RMS,k}$ to be an upsampled version of $\sqrt{\vec{w}_{MS,k}}$ from Eq. 17 and assuming $\vec{w}_{RMS,k}$ is approximately constant over N_Δ samples allows the mean square time history of $\vec{p}_k$ to have approximately the same mean square time history as $\vec{s}_k$. Using this process, $\vec{p}_k$ will also have approximately the same mean square time history as the original extended self noise data.

The assumption that $\vec{w}_{RMS,k}$ will be approximately constant within a time interval Δ_{MS} will be more accurate as the number of samples in the time interval, N_Δ, increases. Let

$$\hat{w}_{d,k} = \frac{1}{N}\sum_{n=1}^{N}\left(\left|\vec{w}_{RMS,k}[n] - \sqrt{\vec{w}_{MS,k}[l]}\right|, \frac{n}{N_\Delta} \le l \le \left(\frac{n-1}{N_\Delta} + 1\right)\right) . \tag{20}$$

Equation 20 gives the mean absolute difference between $\vec{w}_{RMS,k}$ before and after upsampling. Smaller values of $\hat{w}_{d,k}$ represent increased accuracy in the assumption that $\vec{w}_{RMS,k}$ will be approximately constant within a time interval Δ_{MS} and over N_Δ samples. The left side of Fig. 14 shows $\hat{w}_{d,k}$ for different values of N_Δ for band $k = 40$. Values of $\hat{w}_{d,k}$ reduce with increasing N_Δ, but there is a region where values of N_Δ<11 also reduce $\hat{w}_{d,k}$.

Before concluding that small values of N_Δ can be used, the sound pressure variation when N_Δ is small needs to be considered. Let

$$r_{var,k} = \mathrm{Var}\left(\frac{\vec{w}_k}{\vec{w}_{RMS,k}} \cdot \frac{1}{N}\sum_{n=1}^{N} \vec{w}_{RMS,k}[n]\right) . \tag{21}$$

In Eq. 21, $\mathrm{Var}(\vec{x})$ represents the variance over samples of $\vec{x}$. The signal of $\frac{\vec{w}_k}{\vec{w}_{RMS,k}}$ is multiplied by the mean of $\vec{w}_{RMS,k}$ so that $r_{var,k}$ represents the signal variation relative to the case when $\vec{w}_{RMS,k}$ is equal to one Pascal. The right side of Fig. 14 shows that signal variation is low for small values of N_Δ. The case $N_\Delta = 1$ is when $\vec{w}_{RMS,k} = |\vec{w}_k|$, and it has the lowest variation. Signal variation values plateau after $N_\Delta \approx 50$ samples and are comparable to the case when $\vec{w}_{RMS,k}$ is equal to one Pascal.

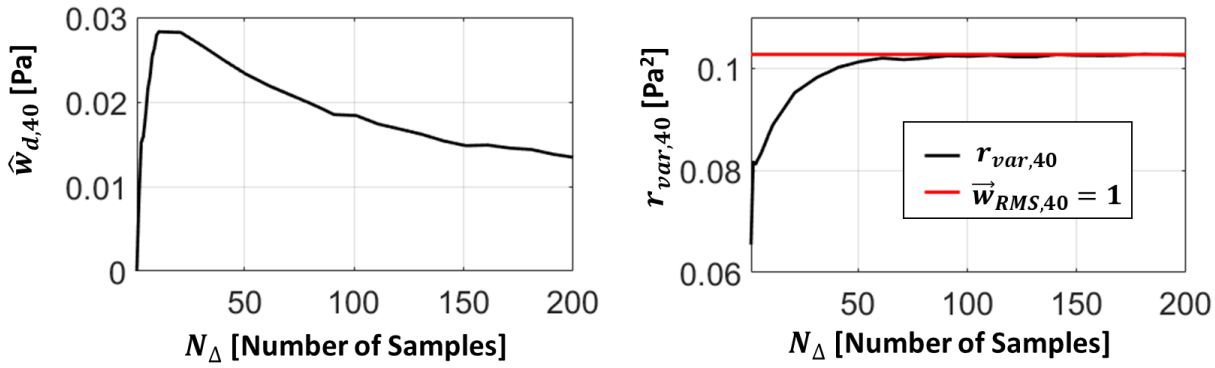

Fig. 14 Upsampling difference and signal variation for $\vec{w}_{RMS,40}$.

Figure 14 suggests large values of N_Δ are preferable. A conclusive study comparing a listener's ability to discern levels of $r_{var,k}$ as a function of N_Δ remains to be investigated. Larger N_Δ values also mean larger Δ_{MS} values for the same sample rate, f_s. Since extended self noise data are provided at time steps of Δ_{MS}, amplitude modulations in the data, which are important to the audible sound, will become suppressed through averaging as Δ_{MS} increases. Therefore, N_Δ must not become large enough to suppress amplitude modulations in the data.

With the method of determining $\vec{w}_{RMS,k}$ now established, Steps 5-8 in Fig. 12 will now briefly be stated. Step 5 uses Eq. 17 to determine $\sqrt{\vec{w}_{MS,k}}$. Step 6 upsamples $\sqrt{\vec{w}_{MS,k}}$ from a sample rate of $1/\Delta_{MS}$ to f_s and generates $\vec{w}_{RMS,k}$. Step 7 executes Eq. 13 now that the time histories of $\vec{s}_k$, $\vec{w}_k$, and $\vec{w}_{RMS,k}$ are available. Each sample of the full audible self noise synthesis signal for the flyover is given in Step 8 by summing over all 1/3 octave band contributions by

$$\vec{p}[n] = \sum_{k=k_1}^{K+k_1-1} \vec{p}_k[n] \,. \tag{22}$$

The sound generated by Eq. 22 will need to be propagated to the ground observer in the NAF with propagation effects.

There are some other notes to consider regarding the stochastic signal modulation method:

1. Since a stochastic signal is applied band by band, there is not one but multiple stochastic signals.
2. The stochastic signal for band k is not $\vec{w}_k$ but $\vec{w}_k/\vec{w}_{RMS,k}$.
3. Normalizing $\vec{w}_k$ by the factor $\sqrt{N}/f_s$ in Eq. 6 provides the convenient method of calculating its mean square value using the ratio of the number of nonzero frequency bins in band k to the length of the signal as computed in Eq. 8. Since $\vec{w}_{RMS,k}$ divides $\vec{w}_k$, another normalization factor may potentially be used to synthesize the self noise.
4. It is unlikely that $\vec{w}_{RMS,k}$ will have a sample value of zero Pascals if Δ_{MS} is much larger than $1/f_s$. In the event a sample of $\vec{w}_{RMS,k}$ does become zero, a routine to set $\vec{p}_k$ to zero at that sample point should be in place.
5. As mentioned earlier, the value of N is chosen so that N/f_s is the duration of the flyover. To reduce data storage, N may be smaller, and the stochastic signals may be repeated to cover the flyover duration. An investigation was not conducted to determine the smallest value of N such that repetitions of the stochastic signals for the bands are unnoticed by most listeners.

VIII. Self Noise Synthesis Validation

A. Verification of synthesized sound pressure level

The stochastic signal modulation method from Section VII was applied to Rotor 1 with a 1.8 mm trailing edge thickness. Figure 10 shows a magnified view of the extended self noise data that modulated the stochastic signal. The

synthesized signal from Eq. 22 was then transformed into a 1/3 octave band time history using Eq. 14 for each band and the same sample time interval as the extended ASNIFM data. This transformation is shown on the right side of Fig. 15, which provides a magnified view of the synthesized signal spanning one rotor revolution starting from two seconds. It is compared with the left side of Fig. 15, which shows the extended ASNIFM self noise data for the same time interval. The synthesis was applied only up to band 43 since the higher 1/3 octave bands contain frequencies beyond the Nyquist frequency. The amplitude modulation lobes of the data were reproduced as well as the appropriate sound pressure levels. The synthesized data on the right is not as smooth as the given ASNIFM self noise data on the left, but the synthesized results were expected to only approximate the given data. Comparisons with other time intervals, other rotors, and other trailing edge thickness cases gave similar results.

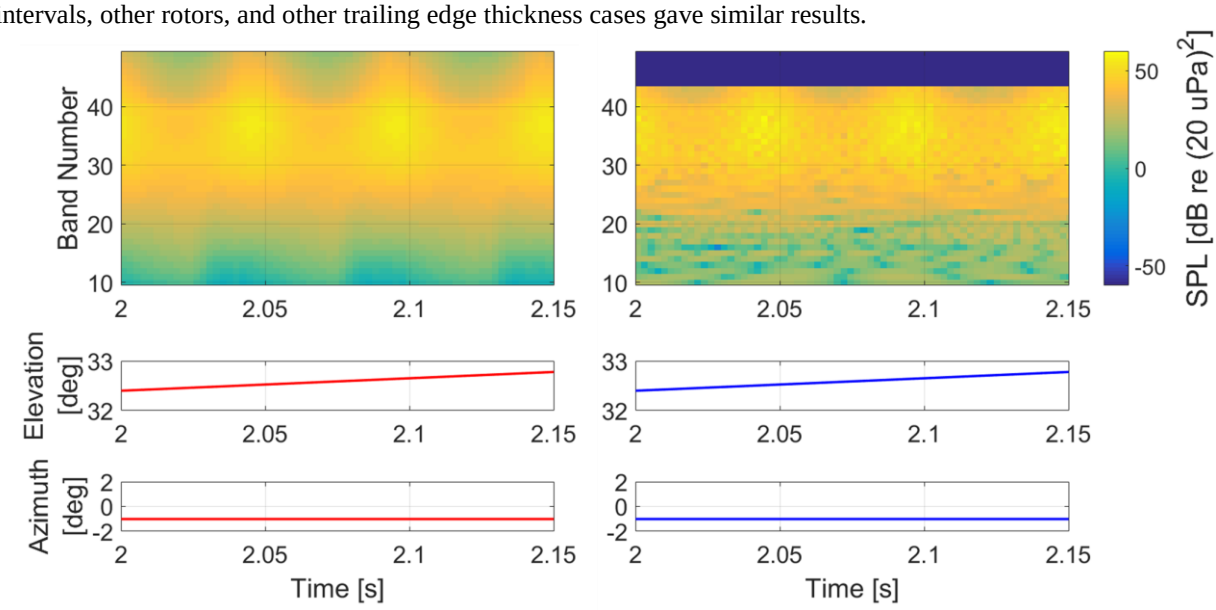

Fig. 15 Comparing self noise data (left) to synthesized spectrum time history (right), Rotor 1, 1.8 mm trailing edge thickness.

Figure 16 shows the synthesized time history for the same time interval from Fig. 15 as well as two other intervals at different emission angles. The self noise amplitude modulation pulses are seen clearly for the interval starting at 2 seconds. The amplitude modulation was less distinct in the ASNFIM data between bands 29 and 40 at emission angles between 80° and 120° (see left plot of Fig. 11). This reduced modulation is apparent in the synthesized sound at 12 seconds in the middle Fig. 16 trace. Above 120°, modulations became more distinct between bands 29 and 34; the slight modulations reappear in the right trace of Fig. 16, with lobes appearing at 22, seconds, 22.05 seconds, and 22.1 seconds. Reduced modulations in the middle and right traces of Fig. 16 are consistent with the ASNIFM prediction.

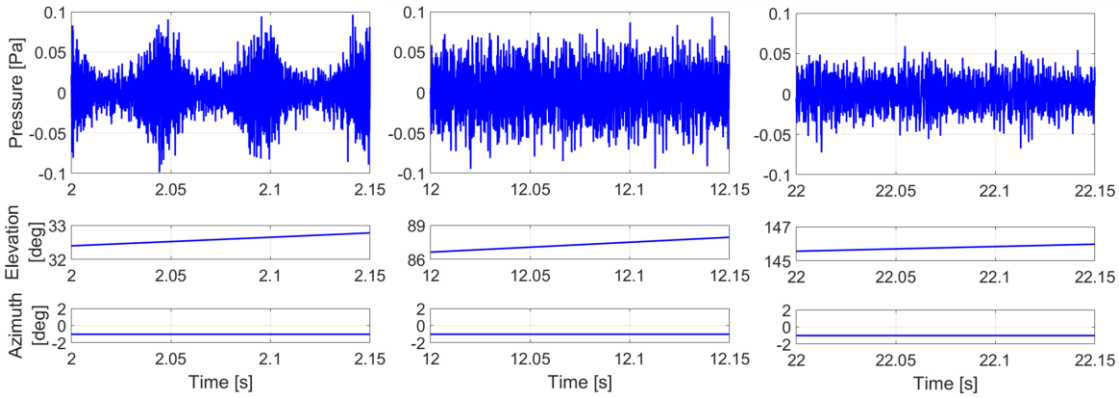

Fig. 16 Synthesized self noise time history, Rotor 1, 1.8 mm trailing edge thickness.

The full audible synthesized self noise sound of Rotor 1 for the 1.8 mm trailing edge thickness case can be found online at Ref. [18]. The beginning of the synthesized sound contains more pronounced modulations readily apparent to a listener. As the synthesized sound progresses, modulation lessens then reappears corresponding to the behavior shown in Fig. 16. As a reminder, the right side of Fig. 15 and the traces in Fig. 16 represent sound before it was propagated to the ground observer.

B. Audible sound fidelity

Although the self noise synthesis process was able to approximately reproduce the same sound pressure levels as the ASNIFM self noise data (as demonstrated in Fig. 15), it is not known if the synthesized sound is what a listener will actually hear from real broadband self noise. Since the eVTOL quadrotor is a concept vehicle, recordings of the vehicle flyover do not exist.

To test the audible fidelity of the self noise synthesis method, a wind tunnel recording of a Straight Up Imaging (SUI) Endurance quadrotor was used as a reference. The SUI Endurance recordings are discussed in Ref. [17]. A broadband self noise recording of rotor 1 (R1) of the quadrotor from a microphone located at elevation emission angle 70° was obtained. The rotor had two blades and a blade passage frequency of approximately 134 Hz. The rotor self noise recording was transformed into a 1/3 octave band spectrum time history similar to the data provided by ASNIFM. A sweep of time intervals for the sound pressure mean square calculation generated a series of spectrum time histories over a single rotor revolution from the recorded data. A different mean square calculation time interval formed each time history. Each time interval was then applied to the self noise synthesis method discussed in Sections VI and VII using the 1/3 octave band time history from the recording as though it came from ASNIFM. One difference from applying the self noise synthesis to the NASA eVTOL quadrotor is that the emission angle for the SUI Endurance sound synthesis remained constant at 70°. No propagation effects were applied. Figure 17 shows magnified views of the synthesis time history results when using Δ_{MS}= 0.23 ms and Δ_{MS}= 3.20 ms. Comparing the results to the recorded time history in the black trace, the Δ_{MS}= 0.23 ms case is visibly closer to the recording.

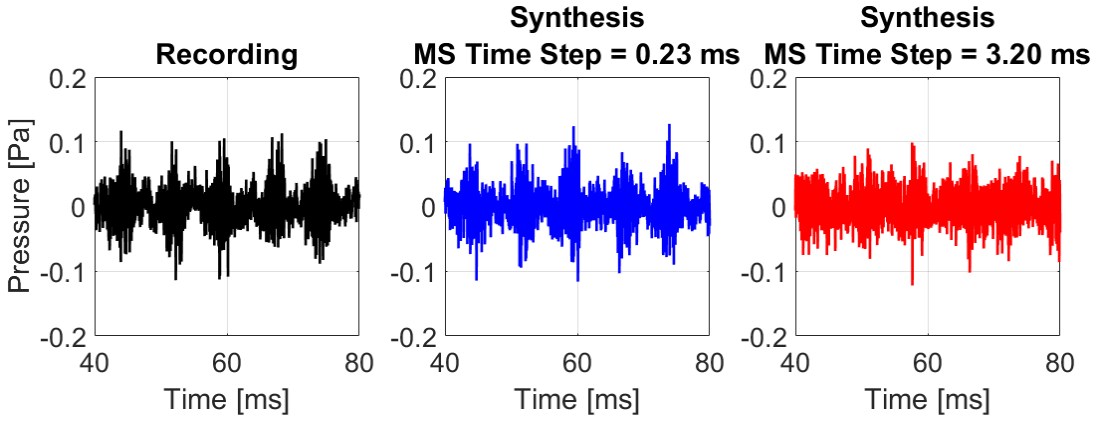

Fig. 17 SUI Endurance self noise synthesis results.

Sounds of the recording, Δ_{MS}= 0.23 ms synthesis, and Δ_{MS}= 3.20 ms synthesis can be found online at Ref. [18]. When listening to the sounds, one may verify that the Δ_{MS}= 0.23 ms synthesis case is audibly close to the recording. In Section VII, it was mentioned that the audible fidelity of the self noise synthesis is dependent on the resolution of the self noise data. Results in Fig. 17 and the corresponding sounds in Ref. [18] demonstrate this relationship.

The Δ_{MS}= 0.23 ms case subjectively validates the self noise synthesis method in terms of audible fidelity. The stochastic signal choice for the synthesis method appears to be appropriate. Further quantitative investigation that may include calculating sound quality metrics between the self noise recording and synthesized sounds still needs to be performed. This quantitative investigation should also include analysis of whether other stochastic signals, such as those with dependence between phases at different frequency bins, may be better suited for the synthesis method.

IX. Auralization Results

A. Baseline Flyover Auralization Results

Periodic and self noise synthesis results from each of the four rotors are propagated using the NAF to a flush ground observer as illustrated in Fig. 2. The propagation proceeded in a uniform atmosphere with temperature of 288.15 Kelvin (15 degrees Celsius), 1 atmospheric pressure, and 70% relative humidity. Auralization of the self noise

from combining the contributions from all four rotors is given in Fig. 18. Figure 19 shows the auralization when the periodic noise from all four rotors are added to the self noise. The results in Figs. 18 and 19 combine contributions from paths 1 and 2, the direct and reflected paths, respectively. Since the observer is flush with the ground, the direct and reflected paths are identical. The azimuth emission angle is zero since the auralization results are with respect to the vehicle center of gravity. In total, the full auralization in Fig. 19 combines 16 contributions (4 rotors x (periodic noise + self noise) x 2 paths). The modulations from the self noise are difficult to see in the spectrogram, but most of the energy content appears to be below 5 kHz. Most of the periodic noise content is also below 5 kHz since a sample rate of 8820 Hz was used in the NAF F1A Synthesis plugin. The auralized sounds from Figs. 18 and 19 can be found online at Ref. [18].

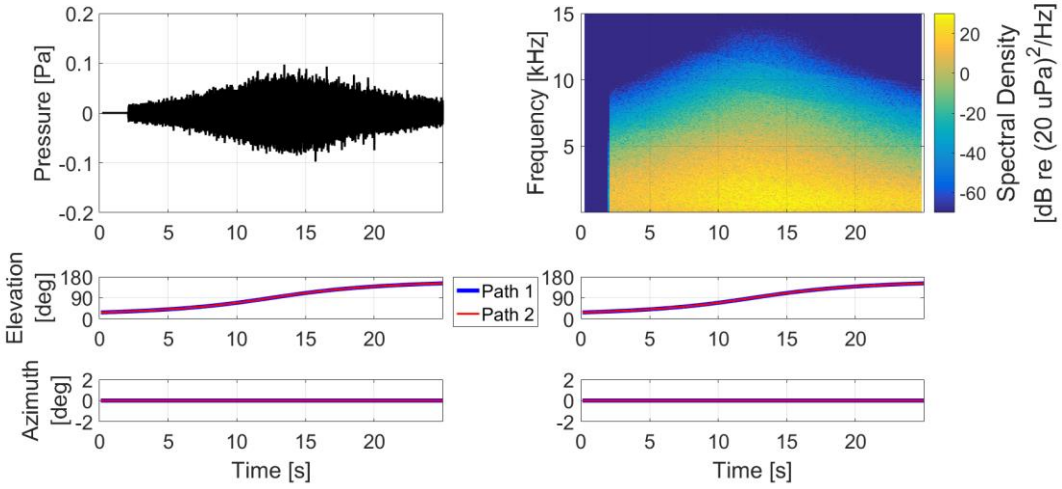

Fig. 18 Auralization of eVTOL quadrotor, self noise only, 1.8 mm trailing edge thickness.

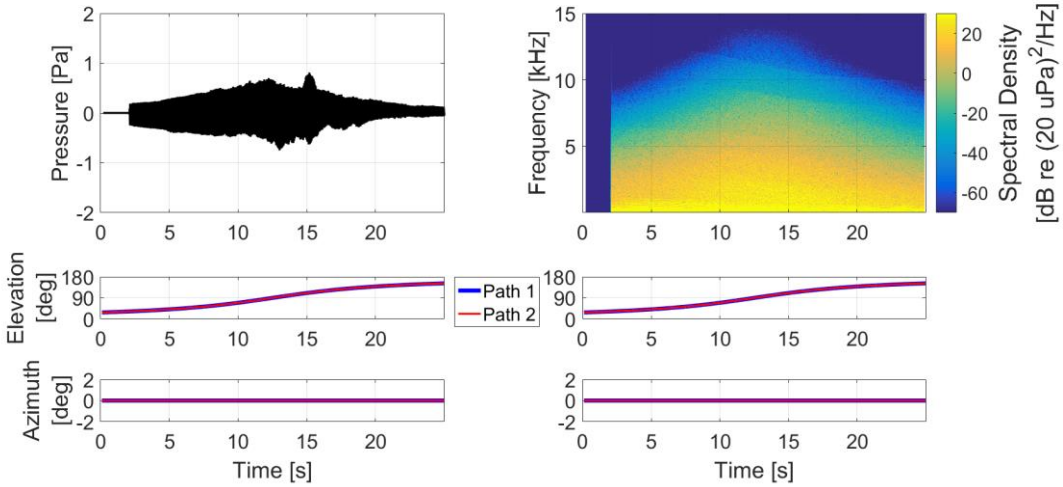

Fig. 19 Auralization of eVTOL quadrotor, 1.8 mm trailing edge thickness.

B. Checking the Auralization

One method to check that the auralized sound pressures generated for the flyover are consistent with the system noise prediction is to compare metrics between the auralization and ANOPP2. Source noise data are propagated to a ground observer using the ANOPP2 Straight Ray Propagation Internal Functional Module (ASRPIFM), and metrics are generated using the ANOPP2 Acoustics Analysis Utility (AAAU). A flowchart depicting the system noise prediction process is provided in Fig. 20. ANOPP2 propagates the periodic and broadband self noise results as 1/3 octave band spectrums without phase information. The propagated values cannot be transformed into audible sound,

but they should be comparable to the auralization sound pressure levels. The overall sound pressure level (OASPL) will be used as the metric for comparison.

To compare with the auralized result, ANOPP2 calculated the OASPL metric at a ground observer for each combination of the four rotors and each noise type (periodic noise, self noise) in isolation from the other noise source combinations. Isolated source calculations were needed to prevent ANOPP2 from using one source hemisphere for the full vehicle, which would eliminate the impact of the separate propagation paths for each source, and OASPL results could not be compared with the auralized results. Therefore, a total of eight OASPL traces (4 rotors x (periodic noise + self noise)) were combined after ANOPP2 calculated each in isolation. Each of the eight OASPL traces already accounted for two propagation paths. The combined OASPL trace from ANOPP2 is shown by the blue trace in Fig. 21.

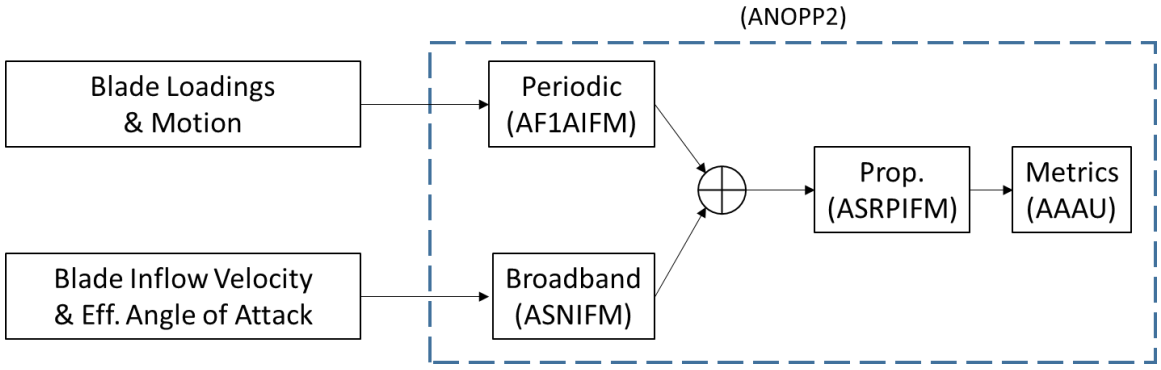

Fig. 20 System noise prediction process.

The auralized sounds from each of the four rotors were also input to AAAU to generate eight OASPL traces (4 rotors x (periodic noise + self noise)). These traces were combined to produce the red trace in Fig. 21. The match between the ANOPP2 and auralization OASPL traces is excellent above 90° elevation with some deviation below 90°. Further investigation suggested that the deviations below 90° come from smaller differences in the ANOPP2 and auralization OASPL traces for periodic noise in Rotor 1 and also for Rotor 2. These OASPL traces are not shown for brevity. Since the differences in the periodic noise ANOPP2 and auralization OASPL traces for each rotor (Rotor 1 and Rotor 2) are small (but not shown) compared to the differences below 90° in Fig. 21, it is concluded that the full OASPL trace agreement between ANOPP2 and the auralization is excellent.

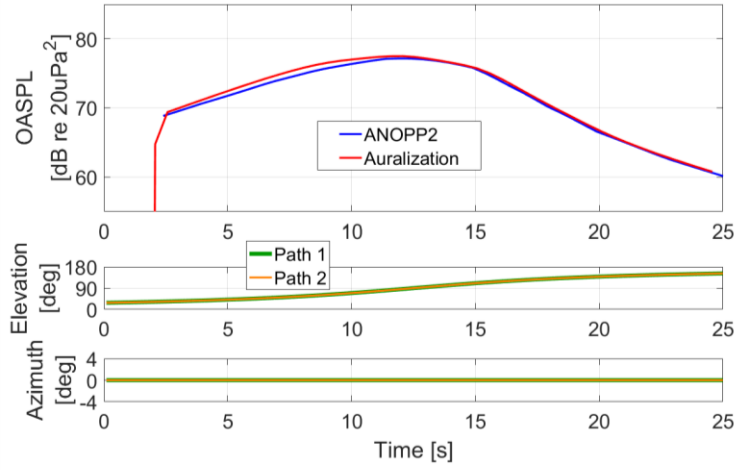

Fig. 21 OASPL trace comparison for eVTOL quadrotor.

C. Auralizations with Different Trailing Edge Thickness

Auralizations were also generated for blades with trailing edge thicknesses of 0.9 mm, 3.6 mm, and 7.2 mm, in addition to the previously discussed case with 1.8mm thickness. Only the ASNIFM self noise data were affected by the different trailing edge thicknesses. For each of the different trailing edge thickness cases, the self noise synthesis

process described in Sections VI and VII was followed, self noise validation comparing synthesized results with ASNIFM data were performed, and the check comparing auralization and ANOPP2 OASPL traces was done. Results of the validations and checks are not given in this paper, but they confirmed that the auralization processes were executed correctly for these other blade trailing edge thickness cases. The final auralization results for each trailing edge thickness case are shown in Fig. 22. Only the spectrograms are shown for each case. Since the results are for the full vehicle auralization, which has an azimuth emission angle of 0° with respect to the vehicle center of gravity, only the elevation emission angle from the vehicle to the ground observer is given.

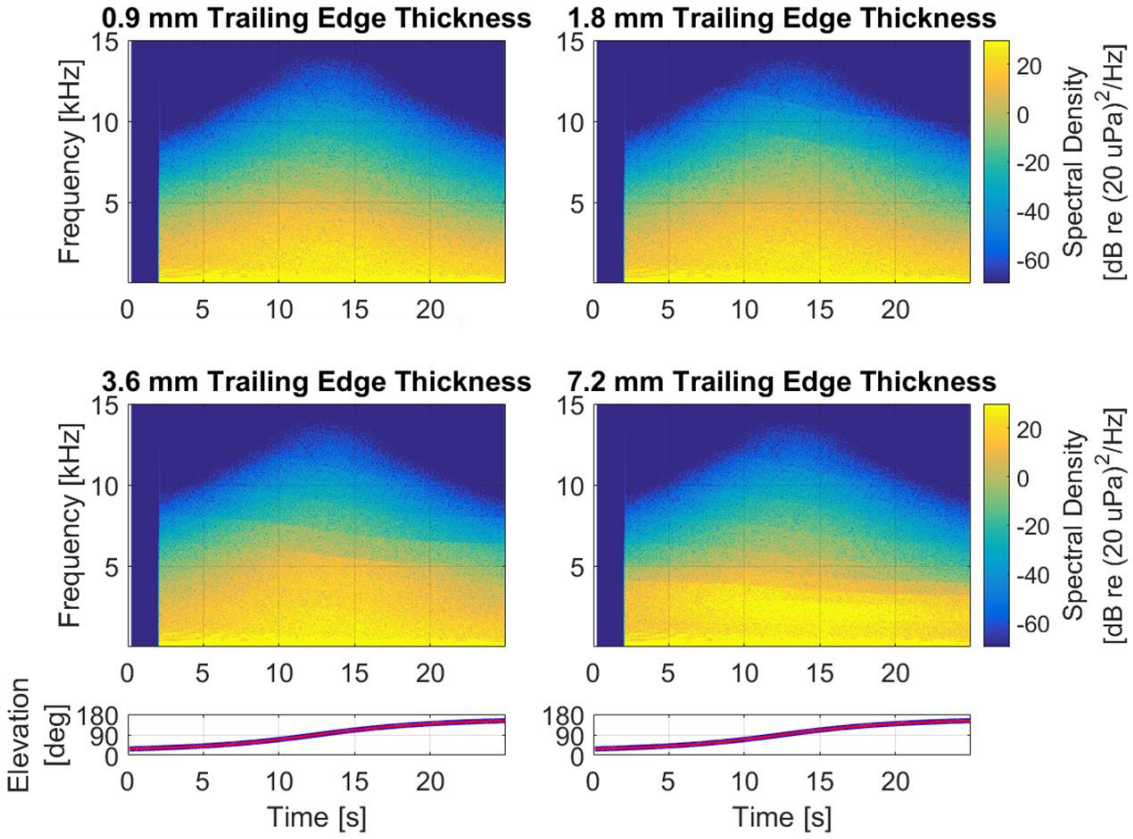

Fig. 22 Auralization results using different trailing edge thicknesses.

The spectrograms in Fig. 22 show the effects of trailing edge thickness on the auralized result. The 1.8 mm trailing edge thickness case spectrogram from Fig. 19 is repeated in the top right of Fig. 22. There was little reduction in the sound pressure levels when the trailing edge thickness was halved to 0.9 mm. More energy became present below 5 kHz when the thickness was doubled to 3.6 mm, but the change from the 1.8 mm trailing edge thickness case is subtle. When the thickness was doubled again to 7.2 mm, the self noise became significantly more noticeable relative to the periodic noise below 5 kHz.

Listening to the auralized sounds from all four cases online in Ref. [18] also reveals how the blade trailing edge thickness can affect the auralized sound. Differences in the audible sound between the 0.9 mm and 1.8 mm cases may not be noticeable for some listeners. Self noise becomes more prominent, audibly, for the 3.6 mm trailing edge thickness, although some listeners may only notice a slight change from the 1.8 mm trailing edge case sound. For the 7.2 mm case, the sound of the auralized flyover has a sound quality distinct from the other three cases.

X. Conclusion

This paper discussed a method to auralize noise from a straight and level flyover of NASA's eVTOL quadrotor vehicle using periodic loading and thickness noise and broadband self noise, for an observer flush with ground. Contributions from all four rotors were included in the auralization. CAMRAD II provided blade input data for the

acoustic predictions. The recently developed NAF F1A Synthesis plugin was used to synthesize the periodic noise contributions from each rotor. A new capability to synthesize modulating broadband self noise from predictions was presented and described in detail. Validation and methods to check the synthesis and auralization results were discussed. A recommendation for future work is to quantify the audible fidelity of the broadband self noise synthesis with available recordings using sound quality metrics. Both the F1A Synthesis plugin and the self noise synthesis capability will be leveraged to auralize other UAM vehicles and be used in perception influenced design.

Results when using four different blade trailing edge thickness values demonstrate the variability of UAM vehicle noise to this design change as the blade trailing edge affected the self noise. When the thickness was made four times the original thickness, the audible sound developed a distinct sound quality different from the other blade thickness cases.

Acknowledgments

Development of the broadband self noise synthesis method was performed with support from the Revolutionary Vertical Lift Technology Project of the NASA Advanced Air Vehicles Program. Integration of the tools for auralization was supported by the Transformational Tools and Technologies Project of the NASA Transformative Aeronautics Concepts Program.

The authors thank Leonard V. Lopes of the NASA Langley Research Center and Jeremy J. Jones of Analytical Mechanics Associates for their assistance with ANOPP2. Thanks also to Brian C. Tuttle of Analytical Mechanics Associates, Inc., for his help with the NAF F1A Synthesis plugin and to Aric R. Aumann of Analytical Services and Materials for his feedback on the broadband self noise synthesis. Thank you to Adrija Bhattacharya of the Georgia Institute of Technology for her work through the NASA Internships, Fellowships and Scholarships program on an early implementation of the broadband self noise synthesis that was leveraged in this work.

References

[1] S. A. Rizzi, D. L. Huff, D. D. Boyd, Jr., P. Bent, B. S. Henderson, K. A. Pascioni, D. C. Sargent, D. L. Josephson, M. Marsan, H. He and R. Snider, "Urban Air Mobility Noise: Current Practice, Gaps, and Recommendations," *NASA/TP–2020-5007433*, October 2020.

[2] S. A. Rizzi and A. K. Sahai, "Auralization of air vehicle noise for community noise assessment.," *CEAS Aeronautical Journal*, vol. 10, no. 1, pp. 313-334, 2019. doi: 10.1007/s13272-019-00373-6.

[3] S. A. Rizzi, "Toward Reduced Aircraft Community Noise Impact via a Perception-Influenced Design Approach," in *Inter-Noise*, Hamburg, Germany, 2016.

[4] J. E. F. Williams and D. L. Hawkings, "Sound Generation by Turbulence and Surfaces in Arbitrary Motion," *Philosophical Transactions of the Royal Society of London. Series A, Mathematical and Physical Sciences*, vol. 264, pp. 321-342, 1969.

[5] T. F. Brook and S. D. Pope, "Airfoil self-noise and prediction," NASA-RP-1218, Hampton, VA, 1989.

[6] N. A. Pettingill and N. S. Zawodny, "Identification and Prediction of Broadband Noise for a Small Quadcopter," in *Proceedings of the Vertical Flight Society 75th Annual Forum*, Philadelphia, 2019.

[7] C. Silva, W. R. Johnson, E. Solis, M. D. Patterson and K. R. Antcliff, "VTOL Urban Air Mobility Concept Vehicles for Technology Development," in *2018 Aviation Technology, Integration, and Operations Conference*, Atlanta, GA, 2018. doi: 10.2514/6.2018-3847.

[8] W. R. Johnson, "NDARC -- NASA Design and Analysis of Rotorcraft, theoretical basis and architecture," in *AHS Aeromechanics Specialists' Conference*, San Francisco, CA, 2010.

[9] W. Johnson, "Comprehensive Analytical Rotorcraft Model of Rotorcraft Aerodynamics and Dynamics, Version 4.10," in *Johnson Aeronautics, Volumes I-9*, 2017.

[10] A. R. Aumann, B. C. Tuttle, W. L. Chapin and S. A. Rizzi, "The NASA Auralization Framework and plugin architecture," in *InterNoise 2015*, San Francisco, CA, USA, 2015.

[11] S. Krishnamurthy, B. C. Tuttle and S. A. Rizzi, "Auralization of Unsteady Rotor Noise using a Solution to the Ffowcs Williams- Hawkings Equation," in *Proceedings of the 75th Annual Forum, Vertical Flight Society*, Philadelphia, 2019.

[12] S. Krishnamurthy, B. C. Tuttle and S. A. Rizzi, "A Synthesis Plug-in for Steady and Unsteady Loading and Thickness Noise Auralization," in *AIAA AVIATION Forum, Paper 2597*, Virtual Event, 2020. doi: 10.2514/6.2020-2597.

[13] F. Farassat and G. P. Succi, "The Prediction of Helicopter Rotor Discrete Frequency Noise," *Vertica*, vol. 7, pp. 309-320, 1983.

[14] L. V. Lopes and C. L. Burley, "ANOPP2 User's Manual," NASA/TM-2016-219342, Hampton, VA, 2016.

[15] M. V. Lowson, "Thoughts on Broad Band Noise Radiation by a Helicopter," Wyle Laboratories, Report WR 68-20, Huntsville, AL, 1971.

[16] A. W. Christian, J. Caston and E. Greenwood, "Regarding the Perceptual Significance and Characterization of Broadband Components of Helicopter Source Noise," in *Proceedings of the Vertical Flight Society 75th Annual Forum*, Philadelphia, PA, 2019.

[17] S. A. Rizzi, N. S. Zawodny and N. A. Pettingill, "On the use of Acoustic Wind Tunnel Data for the Simulation of sUAS Flyover Noise," in *25th AIAA/CEAS Aeroacoustics Conference, Paper 2630*, Delft, The Netherlands, 2019. doi: 10.2514/6.2019-2630.

[18] "Aircraft flyover simulation," NASA, 2020. [Online]. Available: https://stabserv.larc.nasa.gov/flyover/.